Interpenetrating 3D Electrodes for High-Rate Alkaline Water Splitting

Qiu Ren, Longsheng Feng, Cassidy Tran, Samuel Eisenberg, Xinzhe Xue, Anica Pinongcos,

Eric B. Duoss, Cheng Zhu* and Yat Li*

Qiu Ren, Cassidy Tran, Samuel Eisenberg, Xinzhe Xue, Anica Pinongcos, and Yat Li
Department of Chemistry and Biochemistry, University of California, 1156 High Street, Santa Cruz, California 95064, USA
E-mail: yatli@ucsc.edu

Longsheng Feng, Eric B. Duoss and Cheng Zhu
Lawrence Livermore National Laboratory, 7000 East Avenue, Livermore, California 94550, USA
E-mail: zhu6@llnl.gov

*Corresponding authors

Abstract

Mass transfer is critical for the reaction kinetics and efficiency of alkaline water splitting (AWS). For AWS to operate at high current densities (hundreds of mA/cm²), the device architecture must ensure a large catalytic surface area, rapid ion diffusion, and minimal solution and charge transfer resistances. Effective electrodes should also facilitate gas bubble detachment and release. 3D-printed electrodes have shown promise, but stacking them increases ion diffusion length and solution resistance. We demonstrate a new device architecture with interpenetrating gyroid electrodes, providing a large ion-accessible surface area and gas diffusion channels. This design significantly reduces the inter-electrode distance, lowering ion diffusion length and solution resistance. Simulations show faster ion diffusion and higher current density in the interpenetrating configuration compared to separate electrodes. This improved performance, especially at low temperatures and high current densities, highlights a promising strategy for enhancing AWS and other electrochemical systems limited by slow ion diffusion.

ToC Figure

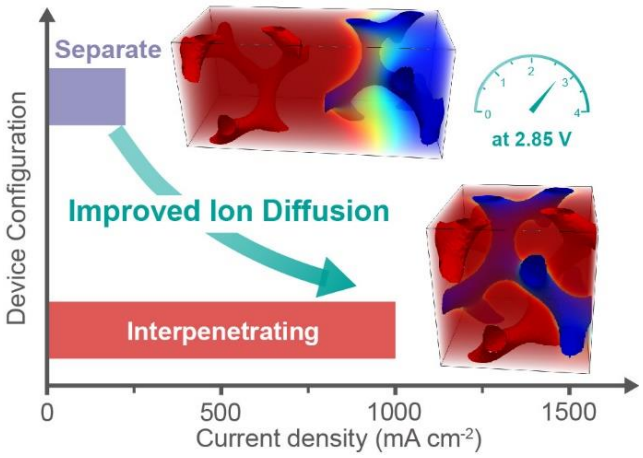

Alkaline water splitting (AWS) is one of the most promising technologies for clean hydrogen production.[1-3] To achieve high efficiency, enormous efforts have been made to minimize the activation overpotential (η_{act}) by increasing electrocatalysts' intrinsic activity and the number of active sites.[4,5] Since AWS involves two gas evolution reactions occurring at the gas-liquid-solid triple phase boundary, its performance is also heavily constrained by additional extrinsic factors, especially at large current densities.[6-8] For instance, the accumulation of generated hydrogen and oxygen gas bubbles will block the electrode's active sites, thus elevating the η_{act} of catalysts. These bubbles will also obstruct the current transport, leading to additional ohmic overpotential (η_{ohm}).[9] With the recent advance in additive manufacturing, various 3D architected electrodes have been fabricated to increase the active surface area and facilitate the bubble's quick detachment and release.[10-12] However, simply stacking 3D electrodes in parallel is not the optimal solution from a device perspective. An important factor that has persistently been neglected is the mass transfer and related ions diffusion resistance during AWS. The efficiency of ion diffusion in the electrolyte depends on the ion concentration gradient and the distance between the anode and the cathode. Thick electrodes and stagnated gas bubbles will add extra distance for ions diffusion or even impede liquid transport, resulting in extended and inhomogeneous concentration gradients and a larger mass transport overpotential (η_{mt}). Current strategies to reduce this resistance mainly focus on increasing the electrolyte conductivity by adding appropriate additives.[13,14] Alternatively, proper arrangement of 3D anodes and cathodes to shorten the inter-electrode distance is another practical and direct approach to enhance ions diffusion at the device level.

Here, we present a new category of interpenetrating gyroids that comprise two independent and disconnected lattices interwoven through the same volume as 3D electrode configuration for AWS. The 3D porous anode and cathode can be integrated while maintaining a constant distance in between, regardless of the thickness of the 3D structure. Notably, the open structure for each single electrode can guarantee the quick release of bubbles in this compact design.[15] In this work, we will use double gyroid interpenetrating Ni lattices as a model system to validate this device concept. Simulation results reveal that ion diffusion between the electrodes is significantly more efficient in the interpenetrating gyroid (3DIG) structure compared to a configuration with separate gyroid electrodes (3DG). The 3DIG device exhibits smaller solution and charge transfer resistances than 3DG. As a result, 3DIG achieves significantly higher current densities than 3DG under the same applied voltage.

The double gyroid interpenetrating structure with a relative density of 30vol% is illustrated in **Figure 1a**. A gyroid lattice is a triple periodic minimal surface structure with zero mean curvature, where two disjointed bicontinuous struts are intertwined with smoothly curved surfaces. Using two lattices of opposite chirality permits the construction of an interpenetrating topology with the two opposite chirality gyroids (Gyroid 1 and Gyroid 2) connected at a subset of their nodes. The high surface-to-volume ratio and the two-phase system are preferable properties for developing 3D electrodes in electrocatalysis applications. **Figure 1b** shows the fabrication process of 3DIG. The interpenetrating double gyroid structure was printed using a commercial photo-curable plant-based resin (Elegoo). Then, we deposited metallic nickel (Ni) onto this polymer substrate using a combination of electroless plating[16] and electrodeposition[17] methods to turn it into a conductive substrate (**Experimental Section**). Ni was also chosen

because it is a widely used catalyst for AWS.[18,19] Notably, part of the supporting structure for the interpenetrating double gyroid structure was covered with tapes during the metallization processes, so Gyroid 1 and Gyroid 2 are two individually addressable Ni electrodes. Once the electrical contacts were made to the two electrodes, the entire 3DIG device was sealed with epoxy to expose only the central interpenetrating gyroid structure for AWS (**Figure 1c**). The digital image (**Figure 1d**) and scanning electron microscopy (SEM) image (**Figure 1e**) show the interpenetrating gyroid structure of 3DIG. The strut thickness of 3DIG is measured to be approximately 650 μm, with a pore size of 2.77 mm. The closest distance between the metallized interpenetrating gyroid electrodes is only 0.2 mm. The electrodes exhibit a smooth surface coating after metallization (**Figure 1f**), and there was no shortage between the electrodes. Energy-dispersive X-ray spectroscopy (EDS) elemental mapping analysis on a 3DIG strut revealed a uniform distribution of Ni signal (**Figure 1g**). X-ray diffraction (XRD) further confirmed the coating is metallic Ni (**Figure S1, Supporting Information**). Taken together, these results support a uniform coverage of Ni on 3DIG. The control sample, 3DG, was prepared using the same printing and metallization method, except the device contains separate Gyroid 1 and Gyroid 2 electrodes (**Figures S2 and S3, Supporting Information**).

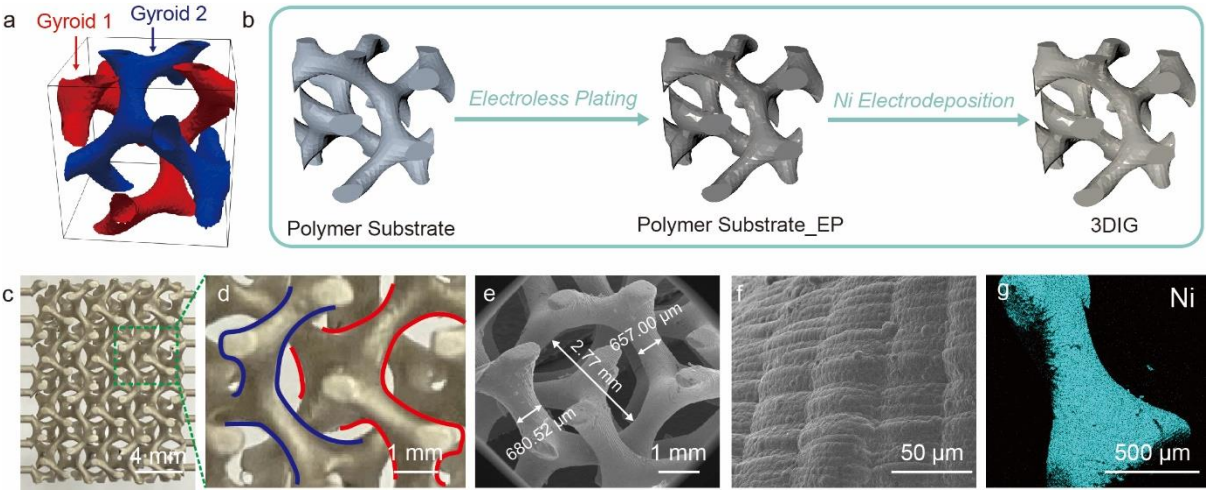

Figure 1. (a) Schematic illustration of an interpenetrating gyroid structure. (b) Schematic diagram showing the fabrication process of 3DIG. (c) Digital image of 3DIG. (d) Magnified image of the region that is highlighted by the box in (c). Gyroid 1 and Gyroid 2 are highlighted with red and blue curves, respectively. (e) SEM image of 3DIG shows the thickness and the pore size. (f) SEM image shows the surface of a 3DIG strut after metallization. (g) EDS elemental mapping of a single 3DIG strut shows uniform distribution of Ni signal.

To explore the impact of the interpenetrating 3D gyroid geometry structure on ionic diffusion, we conducted simulations to track ion concentration within the electrolyte. This was achieved by setting a constant concentration and voltage differential across two electrodes (**Experiment Section**). **Figure 2a** depicts the electrolyte's average ion concentration over time, revealing that the 3DIG structure exhibits significantly faster kinetics and a greater ionic transfer capacity between electrodes. This indicates that the interpenetrating structure not only facilitates quicker ionic diffusion but also effectively utilizes more structure space for ionic transfer. **Figures 2b** and **2c** and **Movies S1 and S2** (**Supporting Information**) further illustrate this by showing the equilibrium concentration distribution in the structure, where a nearly maximum normalized concentration is throughout the 3DIG cell, whereas only three-quarters of the cell achieves saturation in the 3DG cell. This efficient spatial utilization in the 3DIG structure, marked by enhanced kinetics and increased capacity, is attributed to its interpenetrating design, promoting tight spatial integration between electrodes. This integration ensures a uniform electric potential gradient, as demonstrated in **Figure 2d**, unlike the gradient observed for the 3DG in **Figure 2e**. Given that the electric potential gradient primarily drives

ion motion, a consistent and extensive gradient is essential for achieving rapid kinetics and high capacity.

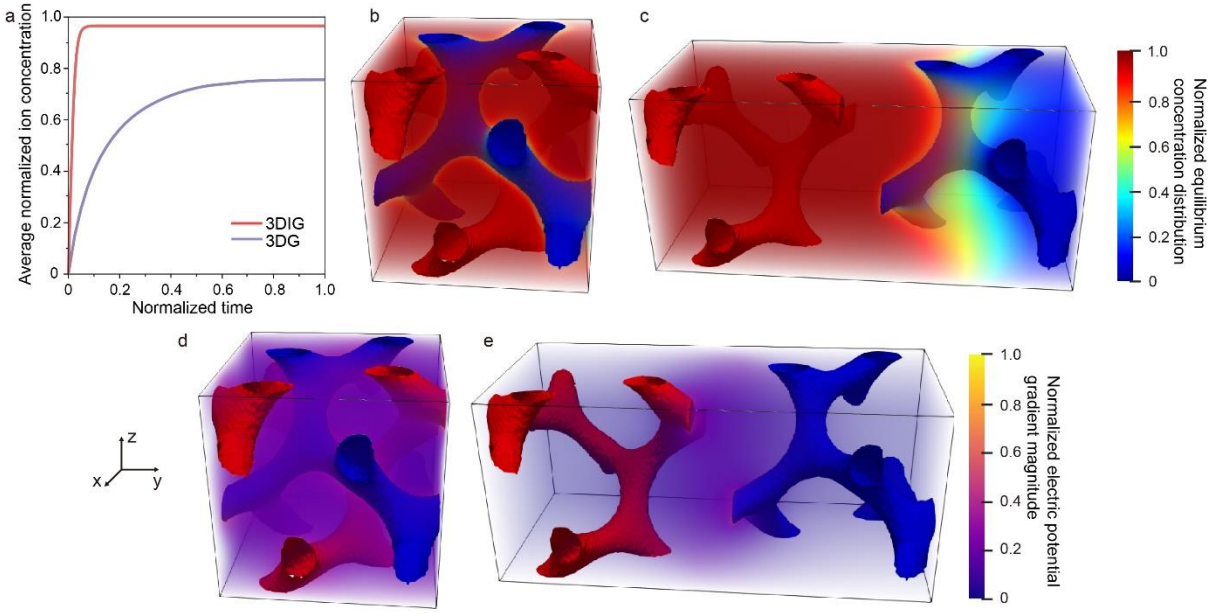

Figure 2. Simulation comparing ion diffusion kinetics in 3DIG and 3DG, driven by constant concentration and electric potential gradients. (a) Average normalized ion concentration in the electrolyte as a function of normalized time. Normalized equilibrium concentration distribution in (b) 3DIG and (c) 3DG. Normalized electric potential gradient magnitude in (d) 3DIG and (e) 3DG.

We prepared several interpenetrating gyroid structures with different feature sizes (length of repeating unit = 8, 6, and 4 mm) to investigate the size effect on their electrochemical activity for AWS (**Figure S4, Supporting Information**). The physical dimensions of these interpenetrating electrodes are listed in **Table S1** (**Supporting Information**). The 3D printing technique also enables the scalability of electrode size (**Figure S5, Supporting Information**).

Choosing these feature sizes is a result of balancing multiple parameters, including the mechanical properties of printed materials, the electrode surface area, the strut thickness, and the inter-electrode distance. Although further reducing the feature size of 3DIG is possible, it is out of the scope of this work. We collected linear sweeping voltammograms (LSVs) from the three 3DIG devices. Among them, the 4 mm device achieves the highest geometric current density under the same applied voltage (**Figure S6a, Supporting Information**). To exclude the effect of surface area, we normalized the current with respect to their electrochemically active surface area (ECSA). Notably, the 4 mm device still shows the highest current density (**Figure S6b, Supporting Information**), suggesting the enhancement is due to the shortening of inter-electrode distance and, thus, ion diffusion length.

To validate the device concept of interpenetrated gyroid structure and the simulation results, we compare the electrochemical performances of 3DIG and 3DG for AWS (**Figure 3**). 3DIG and 3DG were prepared using the same method, so they should have the same surface and intrinsic catalytic properties. Given that they have the same geometric area and the total electrode surface area, they are also expected to have a similar amount of catalytic active sites. The only differences are electrode configuration (interpenetrating vs. separate) and device volume (**Figure S7, Supporting Information**). The compact design of 3DIG reduces the volume by 50% compared to 3DG. 3DG devices with various separations between the two gyroid electrodes were tested (**Figure S8, Supporting Information**), and the 5 mm device was chosen for comparison.

Figure 3a shows that 3DIG reaches an ultrahigh current density of 1000 mA cm^{-2} at 2.85 V, while 3DG only reaches 225 mA cm^{-2} at the same voltage. Since they have similar ECSA

(**Figure S9, Supporting Information**), 3DIG also has a substantially larger ECSA normalized current density than 3DG (**Figure 3b**). Electrochemical impedance spectroscopy (EIS) analysis (**Figure 3c**) suggests the enhanced AWS performance of 3DIG is due to the reduced solution resistance (R_S) and charge transfer resistance (R_{CT}). Note that the two devices were made of the same materials and tested in the same electrolyte (1.0 M KOH), so their electrical resistance should be comparable. Therefore, the R_S and R_{CT} values reflect the ion diffusion efficiency between the two electrodes,[20,21] which is anticipated to be different for the two device configurations. An equivalent circuit model was created to fit the Nyquist plots and estimate the electrodes' R_S and R_{CT} values (**Figures 3d** and **3e**).[22] Significantly, 3DIG exhibits considerably smaller R_S and R_{CT} values than 3DG, indicating more efficient ion diffusion in the interpenetrating configuration, as predicted by simulation. Finally, we also tested 3DIG's electrochemical stability at an applied voltage of 2.4 V. As shown in **Figure 3f**, the initial current density is 366 mA cm^{-2}, and it retains 97 % of its initial value after 100 hours. The results prove that the interpenetrating device structure is mechanically and electrochemically stable for AWS at a practically meaningful current density.

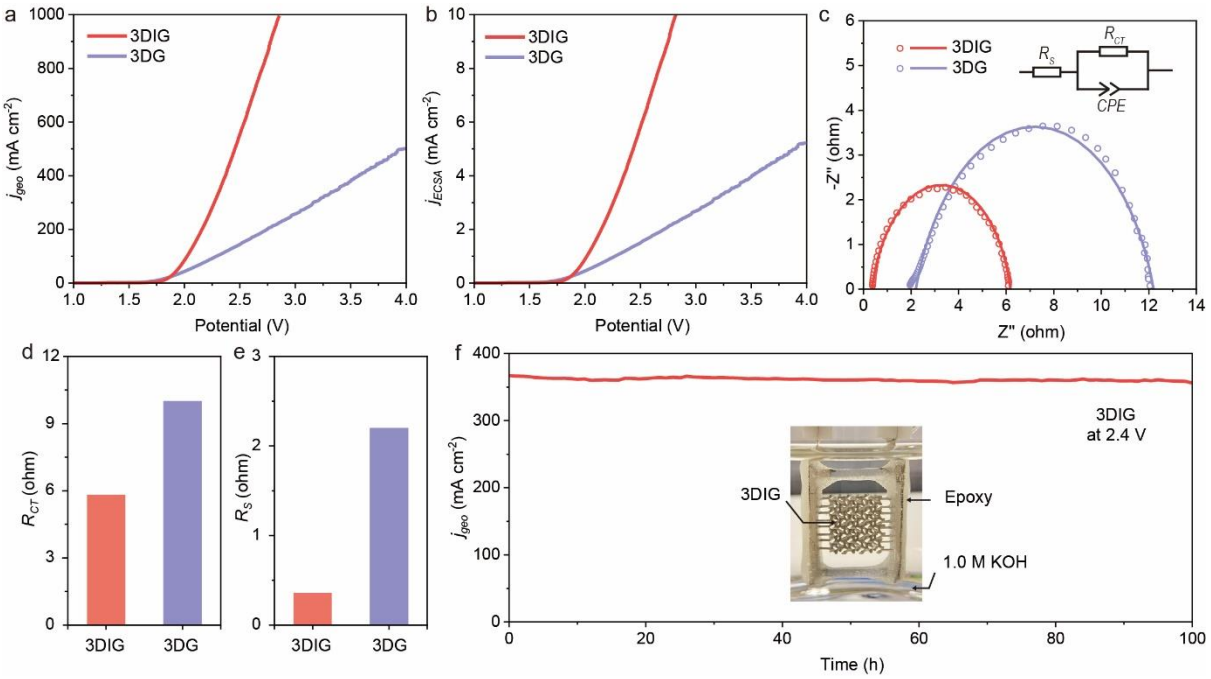

Figure 3. LSVs of 3DIG and 3DG collected in 1.0 M KOH at a scan rate of 1 mV s^{-1} are plotted in (a) geometric current density and (b) ECSA normalized current density. (c) Nyquist plots of 3DIG and 3DG obtained in a frequency region ranging from 100 kHz to 1 Hz under an amplitude of 5 mV. Circles represent experimental data. The solid lines represent fitting curves based on the equivalent circuit model (inset). Histograms show the (d) R_S and (e) R_{CT} values of 3DIG and 3DG. (f) The current density of 3DIG obtained at 2.4 V in 1.0 M KOH is plotted as a function of time. Inset: digital image of 3DIG device during the AWS testing.

Ion diffusion efficiency is known to be temperature dependent. The sluggish ion diffusion at low temperatures poses a significant challenge for many electrochemical reactions, including AWS.[23] The interpenetrating structure could tackle this issue by substantially shortening the inter-electrode distance. We investigated the performance of 3DIG and 3DG at three different temperatures, 275, 298, and 318 K. As shown in **Figure 4a**, both 3DIG and 3DG show a considerable enhancement in AWS performance with the temperature increase, as increasing

temperature helps overcome the reaction barriers and promotes ion diffusion.[24] Notably, 3DIG requires lower voltages to achieve the same current densities as 3DG at all temperatures we studied. The 3DG/3DIG voltage ratios observed at 200 and 400 mA cm^{-2} are plotted as a function of temperature (**Figure 4b**). The two curves show the same trend: the ratio increases with the decrease in temperature, and the voltage ratios obtained at 400 mA cm^{-2} are consistently larger than those obtained at 200 mA cm^{-2} at all temperatures. These results show that the interpenetrating structure plays an even more important role at lower temperatures and higher current densities where ion diffusion is a bigger reaction limiting factor.

Furthermore, EIS analysis was employed to gain a quantitative understanding of the influence of temperature on the ion diffusion efficiency (**Figures 4c** and **4d**). While the resistances increase with the decrease of temperatures for both samples, 3DIG always has substantially smaller R_S and R_{CT} values than 3DG under the same temperature (**Figures 4e** and **4f**). Significantly, 3DIG exhibits fairly small R_S (1 Ω cm^{-2}) and R_{CT} (3.5 Ω cm^{-2}) values even at 275 K, indicating that ion diffusion and charge transfer are efficient. EIS analysis was also conducted at different current densities of 10, 50, 100, and 200 mA cm^{-2} (**Figure S10, Supporting Information**). The R_S values of both devices remained mostly unchanged with increasing current density. On the other hand, their R_{CT} values considerably decrease with the increasing current density because there is a larger driving force for AWS at high current densities.[25,26] While the values of R_{CT} of 3DIG are still smaller than 3DG at all current densities we measured, they become comparable at high current densities. The results suggest the enhanced performance of 3DIG for the high-rate AWS could be primarily due to its considerably smaller R_S value.

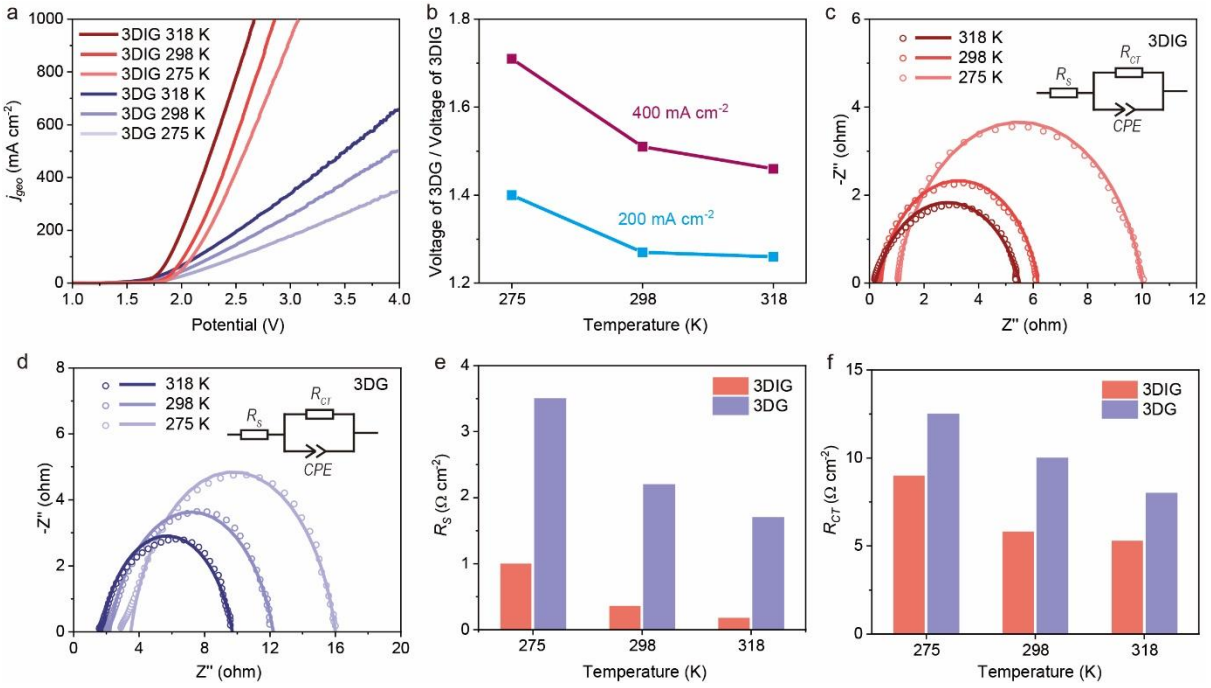

Figure 4. (a) LSVs of 3DIG and 3DG collected in 1.0 M KOH at a scan rate of 1 mV s^{-1} at different temperatures. (b) The 3DG/3DIG voltage ratios obtained at 200 and 400 mA cm^{-2} are plotted as a function of temperature. Nyquist plots of (c) 3DIG and (d) 3DG collected in a frequency range from 100 kHz to 1 Hz at an amplitude of 5 mV at different temperatures. Circles are experimental data. Solid lines are fitting curves based on the equivalent circuit model. Histograms show the (e) R_S, and (f) R_{CT} of 3DIG and 3DG at different temperatures.

To further enhance the AWS performance of 3DIG, we electrodeposited metallic Ni nanocones onto the gyroid electrode surface. Our previous work showed that the nanocone-modified structure can promote gas bubble detachment by turning the electrode surface into underwater superaerophobic.[10] We further decorated the nanocone surface with a layer of NiFeOOH catalyst using a previously reported method.[27] **Figure 5a** shows a digital image of the 3DIG after these modifications (NiFeOOH@3DIG). The shiny surface of 3DIG turned into

a dark grey color. SEM image revealed that the additional coating on the interpenetrating electrodes was uniform and did not cause a shortage (**Figure 5b**). The magnified SEM image confirmed the nanocone-modified surface morphology of NiFeOOH@3DIG (**Figure 5c**). While the NiFeOOH catalyst layer was not observable under SEM, the elemental mapping analysis shows an evenly distributed Fe signal on the strut, proving the successful deposition of a uniform layer of NiFeOOH catalyst (**Figure 5d**). Significantly, NiFeOOH@3DIG shows improved AWS compared to 3DIG by lowering the overpotential (**Figure 5e**).

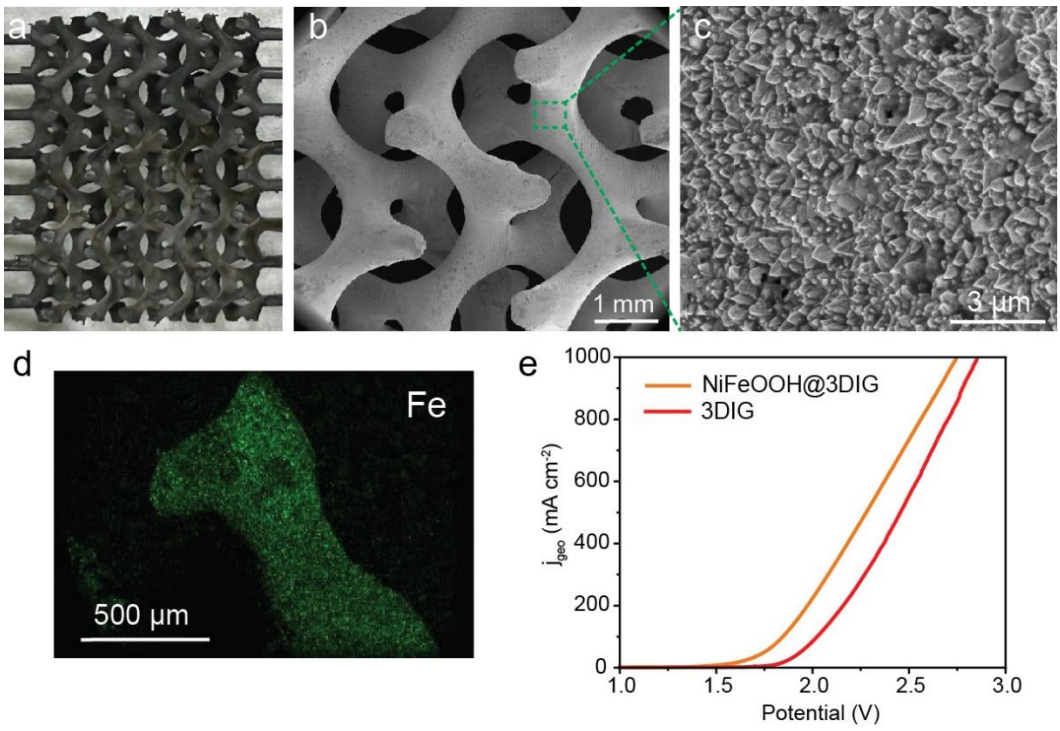

Figure 5. (a) Digital image and (b) SEM image of NiFeOOH@3DIG. (c) Magnified SEM image showing the region highlighted by the box in (b). (d) EDS elemental mapping obtained from a strut of NiFeOOH@3DIG shows the distribution of Fe signal. (e) LSVs of 3DIG and NiFeOOH@3DIG collected in 1.0 M KOH at a scan rate of 1 mV s^{-1}.

In summary, we have demonstrated a new and effective strategy to facilitate ion diffusion for AWS by printing two gyroid electrodes in an interpenetrating configuration. 3D printing of interpenetrating polymer substrate followed by Ni metallization represents a flexible device fabrication method, which can be implemented not only for electrolyzers but also for many other electrochemical systems. The interpenetrating design significantly shortens the ion diffusion length, minimizes R_S, and boosts the rate of achieving concentration equilibrium. All these factors are critical for supporting high-rate AWS. Therefore, 3DIG achieves substantially higher current density than 3DG under the same applied voltage. The advantages of the interpenetrating design are even more obvious at low temperatures where ion diffusion is slower. The AWS performance of the interpenetrating structures can be further improved by optimizing their geometry. For example, adjusting the thickness or shape of the strut can increase surface area and shorten the inter-electrode distance. Additionally, exploring different catalyst coatings may significantly enhance catalytic activity. These optimizations are expected to improve mass transport and interfacial charge transfer, and thus enhance overall electrochemical efficiency. Gas separation represents another challenge for implementing the interpenetrating design in practical applications. One possible solution is to integrate the interpenetrating electrode design with decoupled water electrolysis systems. For example, Dotan *et al.* demonstrated a membrane-free flow electrolyzer, where hydrogen and oxygen evolution reactions are separated into two steps: an electrochemical step and a spontaneous chemical step, enabled by the addition of the $Ni(OH)_2$/NiOOH redox couple.[28] In this design, interpenetrating electrodes could be used for cathode and anode without the need of a separator, as hydrogen and oxygen are generated in different compartments. Another option is to include

a separator or membrane between the interpenetrating electrodes using additive manufacturing methods. This separator would prevent gas mixing and provide channels to collect the gases separately. While this is a technologically challenging task, we are optimistic that advancements in additive manufacturing techniques can overcome this hurdle. Overall, our findings offer a new perspective for designing and fabricating AWS electrolyzer (and other electrochemical device) for supporting high-rate reactions and tackling the challenges of sluggish ion diffusion.

Experimental Section

Chemical reagents

Potassium hydroxide (KOH, Fisher Chemical), sodium hydroxide (NaOH, Aladdin), tin(II) chloride ($SnCl_2$, Aladdin), hydrochloric acid (HCl, 12.0 M), palladium(II) chloride ($PdCl_2$, Sigma), nickel sulfate (NiSO4, Aladdin), citric acid monohydrate ($C_6H_8O_7 \cdot 7H_2O$, Aladdin), sodium hypophosphite ($NaH_2PO_2 \cdot H_2O$, Fisher Chemical) and ammonium chloride (NH_4Cl, Spectrum), nickel (II) chloride hexahydrate ($NiCl_2 \cdot 6H_2O$ Fisher Chemical), iron chloride hexahydrate ($FeCl_3 \cdot 6H_2O$ Fisher Chemical) and ammonium bicarbonate (NH_4HCO_3 Fisher Chemical) were purchased and used directly without further purification.

Structural Characterization

The morphologies of samples were characterized by SEM (Hitachi S-4800 II). The crystal phase of the as-prepared materials was investigated by XRD (Rigaku SmartLab). Elemental

analysis was collected by an SEM equipped with Thermo Fisher Apreo, Oxford Ultimax EDS, Aztec 5.1.

3D Printing of 3DIG and 3DG electrodes

Commercial photo-curable plant-based resin (Elegoo) was used to print interpenetrating and separate double gyroid lattices. A commercial stereolithography printer (Saturn 8K, Elegoo) was used to produce parts. The double gyroid structures presented in this work were generated in a commercial 3D computer graphics and computer-aided design application software (Rhinoceros 3D). All 3D printed parts were rinsed and sonicated in isopropyl alcohol for approximately 5 min. These cleaned parts were post-cured for 1 h at 60 °C by exposing them to 405 nm light (Form Cure, Formlabs). All objects reported in this work were printed with a layer thickness of 50 μm. The duration of the UV exposure was 35 s for the first layer and 5 s for the rest. The retraction velocity of the platform was set at 80 mm min^{-1}. To increase the hydrophilicity of the printed polymers, parts were plasma-treated using an air plasma cleaner (Harrick Plasma) for 2 min at a radio-frequency power of 18 W. Physical dimensions of interpenetrating electrodes with different unit cell lengths are listed in **Table S1** (**Supporting Information**).

Metallization of 3DIG and 3DG

3DIG and 3DG samples were metalized using an electroless Ni plating method followed by an additional step of electrodeposition of Ni, as described in a previously reported method.[16] The as-printed structures were immersed in 300 ml of 1.0 M sodium hydroxide solution at 45 °C

for 30 minutes. Then, they were subsequently submerged in a solution containing 6 g of tin(II) chloride and 6 ml of hydrochloric acid, and then another solution containing 60 mg of palladium(II) chloride and 1.5 ml of hydrochloric acid. The samples were treated in each solution at 45 ℃ for 60 minutes. Following these treatments, electroless Ni plating was conducted by putting the samples in a 300 ml solution composed of 3.9 g of nickel sulfate, 6.3 g of citric acid, and 3.18 g of sodium hypophosphite at 70 ℃ for 10 minutes. The polymer substrate after electroless Ni plating is called Polymer Substrate_EP. The electroless nickel plating process operates through a specific reaction mechanism. Initially, Sn^{2+} ions are absorbed onto the polymer surface through a sensitization process. Subsequently, during activation, Pd nanoparticles serve as catalytic active sites, formed through a redox reaction between Sn^{2+} and Pd^{2+} ($Pd^{2+} + Sn^{2+} \rightarrow Pd + Sn^{4+}$). Following this, when the pre-treated 3D polymer substrates are submerged in a solution containing Ni^{2+} ions and a reducing agent (sodium hypophosphite), initial Ni-P metal nanoparticles adhere to the surface of previously formed Pd nanoparticles. These nanoparticles act as seed crystals, expediting the formation of a continuous and conformal Ni-P conductive layer. To further enhance electric conductivity, electrodeposition of Ni was carried out in a two-electrode system, where Polymer Substrate_EP serves as the working electrode and a piece of Ni foam was used as the counter electrode. The electrolyte solution contains 100 ml of 4 g nickel sulfate and 0.64 g ammonium chloride solution. The electrodeposition was performed at 2 V for 1 hour. Then, the substrate was washed with water and ethanol three times and dried under ambient conditions. The Polymer Substrate_EP after electrodeposition of an additional Ni layer is called 3DIG or 3DG.

Simulation

The diffusion equation (Eqn. 1), accounting for both concentration and potential gradients, is employed to investigate the diffusion kinetics of 3DIG and 3DG cells,

$$\frac{\partial c}{\partial t} = \nabla \cdot \left(D \left[\nabla c + \frac{cZ}{kT} \nabla \phi \right] \right), \quad \text{(Eqn. 1)}$$

where c is concentration, D is ionic diffusivity in the electrolyte, Z is the charge of the ionic species, ϕ is the electric potential field, T is absolute temperature and k is the Boltzmann constant. The electric potential field ϕ follows Poisson's equation (Eqn. 2),

$$\nabla^2 \phi = \frac{\rho}{\epsilon} \quad \text{(Eqn. 2)}$$

where ρ and ϵ are volumetric charge and permittivity. Unit cells of the 3DIG and 3DG structures were respectively utilized as in the simulations. In the 3DG structure, the x and z directions are treated as periodic, while the y direction is fixed to simulate two parallel, separated electrodes. The same boundary conditions were also applied to the 3DIG for fair comparison. We considered a dilute limit for solving the electric field distribution, which was then used as input for the diffusion equation. All simulation parameters (**Table S2**, **Supporting Information**) were non-dimensionalized to enhance the efficiency of numerical solutions.

Electrodeposition of nanocone on 3DIG

The electrode surface of 3DIG was modified to create nanocone Ni structures using a previously reported method.[10] The surface modification was performed in a three-electrode system. 3DIG was used as the working electrode, Ag/AgCl as the reference electrode, and a piece of nickel foam was used as the counter electrode. The electrolyte solution contains 0.84 M nickel (II) chloride hexahydrate, 1.4 M ammonium chloride, and 1 M boric acid. The

electrodeposition was performed at a fixed current density of 20 mA cm^{-2} for 8 min at 60 ℃. The nanocone-modified 3DIG was thoroughly washed with DI water and ethanol and then dried at ambient conditions.

Synthesis of NiFeOOH@3DIG

NiFeOOH catalyst was deposited onto 3DIG using a previously reported method.[27] Nanocone-modified 3DIG was immersed in a solution containing 0.814 mmol iron chloride hexahydrate in 60 ml of ethanol. The samples are then immersed in a solution containing 0.814 mmol iron chloride hexahydrate and 4.49 mmol ammonium bicarbonate in 60 ml of ethanol while stirring for six hours at room temperature to obtain NiFeOOH@3DIG. The sample was removed, washed with DI water, and dried under ambient conditions.

Electrode fabrication

Conductive silver colloidal paint was used to attach a piece of Ni foil strip onto each of the two stands of 3DIG or 3DG, so the two electrodes can be individually addressed. Then, epoxy was used to cover the stands and the rest of the electrode, ensuring that only the central gyroid structure was exposed for water splitting reaction.

Electrochemical measurements

Electrochemical measurements were performed for 3DIG or 3DG on the CHI 660D electrochemical workstation in a two-electrode configuration in a 1.0 M KOH solution. For each sample, cyclic voltammetry (CV) was first performed in a potential window of 0.6 to 3 V

for 40 cycles at a scan rate of 10 mV s^{-1}, and then LSVs were collected at 1 mV s^{-1}. EIS measurements were performed at the voltage corresponding to different current densities (10, 50, 100 and 200 mA cm^{-2}), derived from the LSVs, utilizing a frequency range from 100 kHz to 1 Hz, and an amplitude of 5 mV. The R_S and the R_{CT} were obtained from the Nyquist plots. The water splitting stability test was performed at room temperature in a two-electrode configuration at various voltages. ECSA was determined by measuring the capacitive current associated with double-layer charging from the scan-rate dependence of CVs. LSV and EIS data were collected at various temperatures by placing the electrocatalytic cell in a thermally controlled water bath.

Supporting Information

Supporting Information is available from the ACS Online Library or from the author.

Figures S1-10, including XRD patterns, SEM images, SEM-EDS spectra, digital images, LSV curves, CV curves at different scan rates, and Nyquist plots.

Movies S1-2 show ion diffusion in 3DIG and 3DG.

Author Contributions

Credit: **Qiu Ren** conceptualization, data curation, formal analysis, methodology, visualization, writing - original draft; **Longsheng Feng** methodology, visualization, software, writing original draft, validation; **Cassidy Tran** data curation, visualization, validation, formal analysis, writing - original draft; **Samuel Eisenberg** resources, formal analysis **Xinzhe Xue** resources, formal analysis; **Anica Pinongcos** Resources, data curation; **Eric B. Duoss** Supervision;

Cheng Zhu Conceptualization, funding acquisition, supervision, writing - review & editing; **Yat Li** Conceptualization, funding acquisition, supervision, writing - review & editing.

All authors have given approval to the final version of the manuscript.

Note

The authors declare no competing financial interest.

Acknowledgments

Y.L. thanks the financial support from the Center for Coastal Climate Resilience of the University of California, Santa Cruz (UCSC). This work was performed under the auspices of the U.S. Department of Energy by Lawrence Livermore National Laboratory (LLNL) under Contract No. DE-AC52-07NA27344, through LDRD award 24-ERD-006. IM release number: LLNL-JRNL-862522. L.F. would also like to acknowledge Dr. Tae Wook Heo from LLNL for many valuable discussions on simulation results. The authors thank Drs. Brandon Cheney and Tom Yuzvinsky from UCSC for SEM image acquisition and materials elemental analysis, and acknowledge the W. M. Keck Center for Nanoscale Optofluidics for the use of the FEI Quanta 3D Dual-beam SEM.

References

1. Ehlers, J. C.; Feidenhans'l, A. A.; Therkildsen, K. T.; Larrazábal, G. O., Affordable Green Hydrogen from Alkaline Water Electrolysis: Key Research Needs from an Industrial Perspective. *ACS Energy Lett.* **2023,** *8*, 1502-1509.

2. Yu, Z.-Y.; Duan, Y.; Feng, X.-Y.; Yu, X.; Gao, M.-R.; Yu, S.-H., Clean and Affordable Hydrogen Fuel from Alkaline Water Splitting: Past, Recent Progress, and Future Prospects. *Adv. Mater.* **2021,** *33*, 2007100.

3. Wan, L.; Xu, Z.; Xu, Q.; Pang, M.; Lin, D.; Liu, J.; Wang, B., Key components and design strategy of the membrane electrode assembly for alkaline water electrolysis. *Energy Environ. Sci.* **2023,** *16*, 1384-1430.

4. Clament Sagaya Selvam, N.; Kwak, S. J.; Choi, G. H.; Oh, M. J.; Kim, H.; Yoon, W.-S.; Lee, W. B.; Yoo, P. J., Unveiling the Impact of Fe Incorporation on Intrinsic Performance of Reconstructed Water Oxidation Electrocatalyst. *ACS Energy Lett.* **2021,** *6*, 4345-4354.

5. Zheng, Y.; Serban, A.; Zhang, H.; Chen, N.; Song, F.; Hu, X., Anion Exchange Ionomers Enable Sustained Pure-Water Electrolysis Using Platinum-Group-Metal-Free Electrocatalysts. *ACS Energy Lett.* **2023,** *8*, 5018-5024.

6. Li, Y.; Wei, B.; Yu, Z.; Bondarchuk, O.; Araujo, A.; Amorim, I.; Zhang, N.; Xu, J.; Neves, I. C.; Liu, L., Bifunctional Porous Cobalt Phosphide Foam for High-Current-Density Alkaline Water Electrolysis with 4000-h Long Stability. *ACS Sustainable Chem. Eng.* **2020,** *8*, 10193-10200.

7. Yang, H.; Driess, M.; Menezes, P. W., Self-Supported Electrocatalysts for Practical Water Electrolysis. *Adv. Energy Mater.* **2021,** *11*, 2102074.

8. Kou, T.; Wang, S.; Li, Y., Perspective on High-Rate Alkaline Water Splitting. *ACS Mater. Lett.* **2021,** *3*, 224-234.

9. Luo, Y.; Zhang, Z.; Chhowalla, M.; Liu, B., Recent Advances in Design of Electrocatalysts for High-Current-Density Water Splitting. *Adv. Mater.* **2022,** *34*, e2108133.

10. Ren, Q.; Feng, L.; Ye, C.; Xue, X.; Lin, D.; Eisenberg, S.; Kou, T.; Duoss, E. B.; Zhu, C.; Li, Y., Nanocone-Modified Surface Facilitates Gas Bubble Detachment for High-Rate Alkaline Water Splitting. *Adv. Energy Mater.* **2023,** *13*, 2302073.

11. Kou, T.; Wang, S.; Shi, R.; Zhang, T.; Chiovoloni, S.; Lu, J. Q.; Chen, W.; Worsley, M. A.; Wood, B. C.; Baker, S. E.; Duoss, E. B.; Wu, R.; Zhu, C.; Li, Y., Periodic Porous 3D Electrodes Mitigate Gas Bubble Traffic during Alkaline Water Electrolysis at High Current Densities. *Adv. Energy Mater.* **2020,** *10*, 2002955.

12. Márquez, R. A.; Kawashima, K.; Son, Y. J.; Rose, R.; Smith, L. A.; Miller, N.; Carrasco Jaim, O. A.; Celio, H.; Mullins, C. B., Tailoring 3D-Printed Electrodes for Enhanced Water Splitting. *ACS Appl. Mater. Interfaces* **2022,** *14*, 42153-42170.

13. Ma, T.; Xu, W.; Li, B.; Chen, X.; Zhao, J.; Wan, S.; Jiang, K.; Zhang, S.; Wang, Z.; Tian, Z.; Lu, Z.; Chen, L., The Critical Role of Additive Sulfate for Stable Alkaline Seawater Oxidation on Nickel-Based Electrodes. *Angew. Chem., Int. Ed.* **2021,** *60*, 22740-22744.

14. Beall, C. E.; Fabbri, E.; Schmidt, T. J., Perovskite Oxide Based Electrodes for the Oxygen Reduction and Evolution Reactions: The Underlying Mechanism. *ACS Catal.* **2021,** *11*, 3094-3114.

15. Rocha, F.; Delmelle, R.; Georgiadis, C.; Proost, J., Electrochemical Performance Enhancement of 3D Printed Electrodes Tailored for Enhanced Gas Evacuation during Alkaline Water Electrolysis. *Adv. Energy Mater.* **2022,** *13*, 2203087.

16. Liu, S.; Feng, J.; Bian, X.; Liu, J.; Xu, H.; An, Y., A controlled red phosphorus@Ni–P core@shell nanostructure as an ultralong cycle-life and superior high-rate anode for sodium-ion batteries. *Energy Environ. Sci.* **2017,** *10*, 1222-1233.

17. Zhang, G.; Zhang, X.; Liu, H.; Li, J.; Chen, Y.; Duan, H., 3D-Printed Multi-Channel Metal Lattices Enabling Localized Electric-Field Redistribution for Dendrite-Free Aqueous Zn Ion Batteries. *Adv. Energy Mater.* **2021,** *11*, 2003927.

18. You, B.; Sun, Y., Innovative Strategies for Electrocatalytic Water Splitting. *Acc. Chem. Res.* **2018,** *51*, 1571-1580.

19. Hota, P.; Das, A.; Maiti, D. K., A short review on generation of green fuel hydrogen through water splitting. *Int. J. Hydrogen Energy* **2023,** *48*, 523-541.

20. Ledezma-Yanez, I.; Wallace, W. D. Z.; Sebastián-Pascual, P.; Climent, V.; Feliu, J. M.; Koper, M. T. M., Interfacial water reorganization as a pH-dependent descriptor of the hydrogen evolution rate on platinum electrodes. *Nat. Energy* **2017,** *2*, 17031.

21. Liao, L.; Zhu, J.; Bian, X.; Zhu, L.; Scanlon, M. D.; Girault, H. H.; Liu, B., MoS_2 Formed on Mesoporous Graphene as a Highly Active Catalyst for Hydrogen Evolution. *Adv. Funct. Mater.* **2013,** *23*, 5326-5333.

22. Kou, T.; Chen, M.; Wu, F.; Smart, T. J.; Wang, S.; Wu, Y.; Zhang, Y.; Li, S.; Lall, S.; Zhang, Z.; Liu, Y. S.; Guo, J.; Wang, G.; Ping, Y.; Li, Y., Carbon doping switching on the hydrogen adsorption activity of NiO for hydrogen evolution reaction. *Nat. Commun.* **2020,** *11*, 590.

23. Tang, X.; Gao, W.; Wu, Z.; Wan, T.; Shen, Q.; Kong, X.; Li, K.; Wu, H., Ni(II) Complex Based on Imidazole Dicarboxylic Acid as a Promising Electrocatalyst for Hydrogen Evolution Reaction and H_2O_2-Sensing. *Electrocatalysis* **2024,** 1-12.

24. Jang, M. J.; Yang, S. H.; Park, M. G.; Jeong, J.; Cha, M. S.; Shin, S.-H.; Lee, K. H.; Bai, Z.; Chen, Z.; Lee, J. Y.; Choi, S. M., Efficient and Durable Anion Exchange Membrane Water

Electrolysis for a Commercially Available Electrolyzer Stack using Alkaline Electrolyte. *ACS Energy Lett.* **2022,** *7*, 2576-2583.

25. Siracusano, S.; Trocino, S.; Briguglio, N.; Baglio, V.; Aricò, A. S. Electrochemical Impedance Spectroscopy as a Diagnostic Tool in Polymer Electrolyte Membrane Electrolysis. *Materials* **2018**, *11*, 1368.

26. Huo, X.; Shan, G.; Yang, L.; Gao, L.; Wang, Y.; Zhang, M.; Fu, Y.; Li, W.; Zhang, J., Impedance analysis of alkaline water electrolysis based on distribution of relaxation time. *Int. J. Hydrogen Energy* **2024**, *53*, 684-697.

27. Zhou, H.; Yu, F.; Zhu, Q.; Sun, J.; Qin, F.; Yu, L.; Bao, J.; Yu, Y.; Chen, S.; Ren, Z., Water splitting by electrolysis at high current densities under 1.6 volts. *Energy Environ. Sci.* **2018**, *11*, 2858-2864.

28. Yan, X.; Biemolt, J.; Zhao, K.; Zhao, Y.; Cao, X.; Yang, Y.; Wu, X.; Rothenberg, G.; Yan, N., A membrane-free flow electrolyzer operating at high current density using earth-abundant catalysts for water splitting. *Nat. Commun.* **2021**, *12*, 4143.